Technical Report ARWSB-TR-16005

Fatigue Crack Growth Behavior and Microstructural Mechanisms in Ti-6Al-4V Manufactured by Laser Engineered Net Shaping

Yuwei Zhai*
Diana A. Lados*
Eric J. Brown
Gregory N. Vigilante

* Worcester Polytechnic Institute, Integrative Materials Design Center, 100 Institute Road
Worcester, MA 01609

December 2015

U.S. ARMY ARMAMENT RESEARCH, DEVELOPMENT AND
ENGINEERING CENTER
Weapons and Software Engineering Center
U.S. Army Benét Laboratories

REPORT DOCUMENTATION PAGE

Form Approved
OMB No. 0704-0188

1. REPORT DATE *(DD-MM-YYYY)*	2. REPORT TYPE	3. DATES COVERED *(From - To)*
Dec 2015	Technical Report	

4. TITLE AND SUBTITLE
Fatigue Crack Growth Behavior and Microstructural Mechanisms in Ti-6Al-4V Manufactured by Laser Engineered Net Shaping

5a. CONTRACT NUMBER

5b. GRANT NUMBER

5c. PROGRAM ELEMENT NUMBER

6. AUTHOR(S)
Yuwei Zhai*
Diana A. Lados*
Eric J. Brown
Gregory N. Vigilante

5d. PROJECT NUMBER

5e. TASK NUMBER

5f. WORK UNIT NUMBER

7. PERFORMING ORGANIZATION NAME(S) AND ADDRESS(ES)
U.S. Army ARDEC
Benet Laboratories, RDAR-WSB
Watervliet, NY 12189-4000

8. PERFORMING ORGANIZATION REPORT NUMBER
ARWSB-TR-16005

9. SPONSORING/MONITORING AGENCY NAME(S) AND ADDRESS(ES)

10. SPONSOR/MONITOR'S ACRONYM(S)

11. SPONSORING/MONITORING AGENCY REPORT NUMBER

12. DISTRIBUTION AVAILABILITY STATEMENT
Approved for public release; distribution is unlimited

13. SUPPLEMENTARY NOTES
*Worcester Polytechnic Institute, Integrative Materials Design Center, 100 Institute Road, Worcester, MA 01609

14. ABSTRACT
Laser engineered net shaping (LENS) is an additive manufacturing technique developed specifically for fabricating metallic materials, such as steel, titanium alloys, and nickel-based superalloys, which are widely used in critical structural components. The layering procedure, cyclic heating, and fast cooling during LENS generate unique microstructural features and mechanical properties. Numerous research studies have been conducted mainly in areas including process-related simulation, microstructure characterization, and the performance of LENS fabricated materials under static loading conditions. The fatigue and fatigue crack growth properties and mechanisms in LENS materials, however, have not been thoroughly investigated. In this study, long fatigue crack growth tests were conducted at two stress ratios (R=0.1 and 0.8), using Ti-6Al-4V fabricated by different LENS processing parameters, in both as-fabricated and heat treated conditions. Data and fundamental knowledge that facilitate the application of LENS in the design and repair of structural components were generated in this study and will be systematically discussed.

15. SUBJECT TERMS
LENS, Ti-6Al-4V, Microstructure, Long and small fatigue crack growth, Fatigue crack growth mechanisms

16. SECURITY CLASSIFICATION OF:			17. LIMITATION OF ABSTRACT	18. NUMBER OF PAGES	19a. NAME OF RESPONSIBLE PERSON
			U	22	G.N. Vigilante
a. REPORT U/U	**b. ABSTRACT** U	**c. THIS PAGE** U			**19b. TELEPONE NUMBER** *(Include area code)* (518) 266-5204

Standard Form 298 (Rev. 8-98)
Prescribed by ANSI-Std Z39-18

INSTRUCTIONS FOR COMPLETING SF 298

1. REPORT DATE. Full publication date, including day, month, if available. Must cite at lest the year and be Year 2000 compliant, e.g., 30-06-1998; xx-08-1998; xx-xx-1998.

2. REPORT TYPE. State the type of report, such as final, technical, interim, memorandum, master's thesis, progress, quarterly, research, special, group study, etc.

3. DATES COVERED. Indicate the time during which the work was performed and the report was written, e.g., Jun 1997 - Jun 1998; 1-10 Jun 1996; May - Nov 1998; Nov 1998.

4. TITLE. Enter title and subtitle with volume number and part number, if applicable. On classified documents, enter the title classification in parentheses.

5a. CONTRACT NUMBER. Enter all contract numbers as they appear in the report, e.g. F33615-86-C-5169.

5b. GRANT NUMBER. Enter all grant numbers as they appear in the report, e.g. 1F665702D1257.

5c. PROGRAM ELEMENT NUMBER. Enter all program element numbers as they appear in the report, e.g. AFOSR-82-1234.

5d. PROJECT NUMBER. Enter al project numbers as they appear in the report, e.g. 1F665702D1257; ILIR.

5e. TASK NUMBER. Enter all task numbers as they appear in the report, e.g. 05; RF0330201; T4112.

5f. WORK UNIT NUMBER. Enter all work unit numbers as they appear in the report, e.g. 001; AFAPL30480105.

6. AUTHOR(S). Enter name(s) of person(s) responsible for writing the report, performing the research, or credited with the content of the report. The form of entry is the last name, first name, middle initial, and additional qualifiers separated by commas, e.g. Smith, Richard, Jr.

7. PERFORMING ORGANIZATION NAME(S) AND ADDRESS(ES). Self-explanatory.

8. PERFORMING ORGANIZATION REPORT NUMBER. Enter all unique alphanumeric report numbers assigned by the performing organization, e.g. BRL-1234; AFWL-TR-85-4017-Vol-21-PT-2.

9. SPONSORING/MONITORS AGENCY NAME(S) AND ADDRESS(ES). Enter the name and address of the organization(s) financially responsible for and monitoring the work.

10. SPONSOR/MONITOR'S ACRONYM(S). Enter, if available, e.g. BRL, ARDEC, NADC.

11. SPONSOR/MONITOR'S REPORT NUMBER(S). Enter report number as assigned by the sponsoring/ monitoring agency, if available, e.g. BRL-TR-829; -215.

12. DISTRIBUTION/AVAILABILITY STATEMENT. Use agency-mandated availability statements to indicate the public availability or distribution limitations of the report. If additional limitations/restrictions or special markings are indicated, follow agency authorization procedures, e.g. RD/FRD, PROPIN, ITAR, etc. Include copyright information.

13. SUPPLEMENTARY NOTES. Enter information not included elsewhere such as: prepared in cooperation with; translation of; report supersedes; old edition number, etc.

14. ABSTRACT. A brief (approximately 200 words) factual summary of the most significant information.

15. SUBJECT TERMS. Key words or phrases identifying major concepts in the report.

16. SECURITY CLASSIFICATION. Enter security classification in accordance with security classification regulations, e.g. U, C, S, etc. If this form contains classified information, stamp classification level on the top and bottom of this page.

17. LIMITATION OF ABSTRACT. This block must be completed to assign a distribution limitation to the abstract. Enter UU (Unclassified Unlimited) or SAR (Same as Report). An entry in this block is necessary if the abstract is to be limited.

Abstract

Laser engineered net shaping (LENS) is an additive manufacturing technique developed specifically for fabricating metallic materials, such as steel, titanium alloys, and nickel-based superalloys, which are widely used in critical structural components. The layering procedure, cyclic heating, and fast cooling during LENS generate unique microstructural features and mechanical properties. Numerous research studies have been conducted mainly in areas including process-related simulation, microstructure characterization, and the performance of LENS fabricated materials under static loading conditions. The fatigue and fatigue crack growth properties and mechanisms in LENS materials, however, have not been thoroughly investigated. In this study, long fatigue crack growth tests were conducted at two stress ratios (R=0.1 and 0.8), using Ti-6Al-4V fabricated by different LENS processing parameters, in both as-fabricated and heat treated conditions. Microstructurally-small fatigue crack growth testing was also conducted. Both long and small fatigue crack growth mechanisms were established. Data and fundamental knowledge that facilitate the application of LENS in the design and repair of structural components were generated in this study and will be systematically discussed.

Keywords: LENS, Ti-6Al-4V, Microstructure, Long and small fatigue crack growth, Fatigue crack growth mechanisms

Nomenclature	
a_n	Notch length (measured from pin hole)
a_i	Initial crack length
a	Current crack length
w	Compact tension specimen width
B	Compact tension specimen thickness
R	Stress ratio
ΔK_i	Initial stress intensity factor range
c	K-gradient used during fatigue crack growth testing
ACR	Adjusted compliance ratio method used for closure correction
ΔK_{app}	Applied stress intensity factor range
$\Delta K_{eff-ACR}$	Effective stress intensity factor range calculated with ACR
ΔK_{th}	Threshold stress intensity factor
ΔK_{FT}	Plain-strain fracture toughness
AF	As LENS fabricated condition
HT	Post-LENS heat treated condition
LP	Low power fabricated condition
HP	High power fabricated condition

TABLE OF CONTENTS

LIST OF FIGURES

LIST OF TABLES

1. Introduction

Laser engineered net shaping (LENS) is an additive manufacturing technique developed at Sandia National Laboratories for the direct fabrication of metallic components. Using this technique, fabrication of metal parts directly from 3D CAD models using metal powder is feasible. The operational principle of LENS is schematically represented in Fig. 1. Metal powder is injected into a molten pool created on a substrate by a focused, high power laser beam, while the x-y table controls the planar motion (for 3-axis systems, 5-axis systems also allow for rotation parallel and about the x and y axes) of the substrate to achieve the selective deposition of powder based on the designed cross-sectional geometry. The laser beam moves coaxially with the powder delivery nozzles in the z direction, allowing for the fabrication of consecutive layers. LENS technique permits the creation of intricate geometries, reduces manufacturing lead-time and material waste, and offers great convenience in repair, offering great benefits once utilized in critical applications such as medical, aircraft, and ground transportation industries [1].
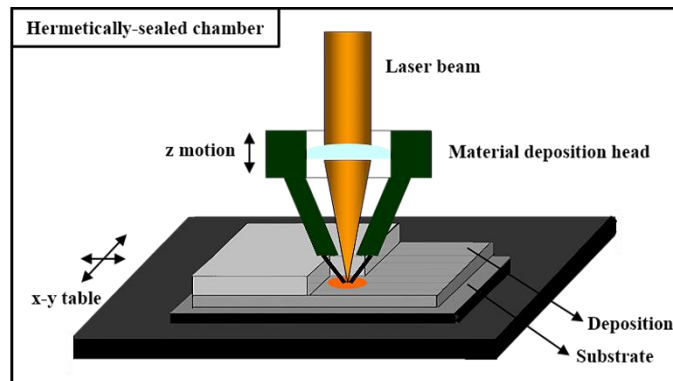
Fig. 1. Schematic representation of LENS.

Research have been carried out to understand the LENS process, as well as the microstructure and mechanical properties of LENS fabricated materials [2-10]. Griffith et al. [2,3] were among the first researchers who conducted systematic studies on LENS using materials ranging from stainless steels to titanium alloys to nickel-based superalloys. It was concluded that in most cases, LENS materials yield mechanical properties comparable to those conventionally manufactured, and that it was possible to optimize the processing parameters to improve fabrication and properties. Wu et al. [4-8] performed a series of experiments using LENS titanium alloys, and observed that the morphologies and size of the typical columnar grains and lamellar microstructures are largely affected by laser power and scanning speed. Kelly and Kampe [9,10] conducted in-depth studies on the microstructure evolution of laser deposited Ti-6Al-4V, and developed a computational thermal model to simulate the LENS process and predict the microstructure.

Despite the extensive work conducted pertaining to the characterization of microstructure and mechanical properties of LENS materials, a major focus has been on their static properties. Limited work can be found discussing the fatigue-related performance [11-14], which is critical in structural design and applications. Amsterdam and Kool [11] performed high cycle fatigue tests on LENS Ti-6Al-4V and Inconel 718. Although porosity was observed in both laser deposited materials, their fatigue performance was found comparable to their wrought counterparts. Kobryn and Semiatin [12] conducted a systematic investigation on the fatigue and fatigue crack growth performance of laser deposited Ti-6Al-4V. Severe lack-of-fusion porosity was observed between deposition layers, which was the major cause for anisotropy in mechanical properties and lower fatigue strength and fracture toughness compared to wrought materials. Hot isostatic pressing (HIP) eliminated the lack-of-fusion porosity, and yielded comparable fatigue strength in laser deposited Ti-6Al-4V to that of wrought products. Ganesh et al. [14] compared the fatigue crack growth

rates of laser rapid manufactured and wrought In-625 alloys. It was noted that fatigue crack growth is slower in laser rapid manufactured material in the Paris regime, and is comparable between the two alloys at higher ΔK levels. Several other studies were conducted using materials fabricated by different additive manufacturing techniques [15-23]. Brandl et al. [15] studied the high cycle fatigue and fracture behavior of Al-Si-10Mg alloy manufactured by selective laser melting (SLM). It was observed that porosity and peak-hardening heat treatment were the controlling factors of the fatigue resistance, while testing directions have the least impact. Leuders et al. [16] conducted in-depth studies of the fatigue crack growth behavior in SLM Ti-6Al-4V in both as built and heat treated conditions. The fatigue crack propagation mechanisms were also correlated to the microstructure by (electron backscatter diffraction) EBSD analysis. It was determined that the martensitic α' phase was unfavorable and could be tailored by heat treatment. It was also observed that porosity influenced primarily the Region I of fatigue crack growth, while the internal stress mainly affected the subsequent phases of crack growth. Edwards and Ramulu [21] evaluated the fatigue properties of Ti-6Al-4V manufactured by electron beam melting (EBM). It was observed that EBM Ti-6Al-4V had similar fatigue crack growth behavior to wrought Ti-6Al-4V in Region I of crack growth, and slower fatigue crack propagation rates in Regions II and III.

The present work aims to contribute to the emerging fatigue crack growth databases for additively manufactured materials, as well as to establish the fatigue crack propagation mechanisms at the microstructural scale. Ti-6Al-4V is of interest, considering the alloy's high specific strength, corrosion resistance, and good biocompatibility which lead to broad applications. Samples were fabricated using various LENS processing parameters and were further subjected to post-LENS heat treatment, in order to study their effects on the microstructure and mechanical properties of LENS Ti-6Al-4V. Both long and microstructurally-small fatigue crack growth tests were conducted such that a full-scale understanding of the fatigue crack propagation behavior and mechanisms in LENS Ti-6Al-4V could be established.

In order to support subsequent discussions, the differences between long, physically-small, and microstructurally-small cracks are briefly introduced here. Fatigue cracks are categorized based on their relative dimensions, namely, crack length (a) and width (w) to the length of the shielding zone (l_s), and the characteristic microstructure size (m_s) of the material, as illustrated in Figs. 2(a-c) [24,25]. Long cracks, Fig. 2(a), grow purely under elastic fields and sample the microstructure in a continuous way. Their propagation can be analyzed by linear elastic fracture mechanics (LEFM). Physically-small cracks, Fig. 2(b), although considered long in terms of continuum mechanics and LEFM analyses, may propagate at faster rates than long cracks with limited shielding zones (l_s), i.e., closure effects [26,27]. The growth of microstructurally-small cracks, Fig. 2(c), is greatly influenced by the material's characteristic microstructural dimensions (m_s) [27,28]. Microstructurally-small cracks tend to have a lower stress intensity factor threshold and grow at a faster rate than physically-small and long cracks in the same material during early propagation stages [27-30]. The differences in the fatigue crack growth behavior of these cracks, especially in the threshold regime and early growth stages, is illustrated in Fig. 2(d). This implies that the use of only long fatigue crack growth data in estimating the life span of components may be non-conservative in some cases [26,27], and emphasizes the importance of a full-scale understanding of fatigue crack growth behavior in materials, including those fabricated by additive manufacturing.
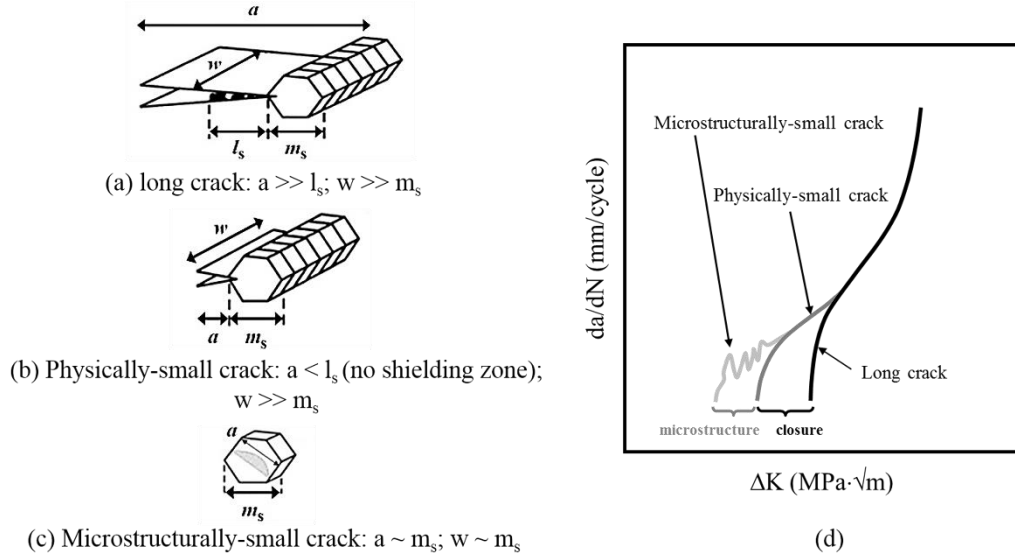
Fig. 2. Definitions of (a) long (b) physically-small (c) microstructurally-small cracks; and (d) qualitative comparison in fatigue crack growth behavior between theses cracks [24,25].

2. Experimental methodology

2.1. Fabrication of LENS depositions

LENS depositions were fabricated at Benét Laboratories, using an Optomec LENS 850-R system. The powder precursor was Crucible Research's GA (gas atomized) Ti-6Al-4V spherical powder (-100/+325 mesh size), which was selectively deposited in a cross-hatched manner with a 90° hatching angle between alternating layers. The LENS depositions were fabricated using two power levels, low and high, and the detailed processing parameters are shown in Table 1.

Table 1
Processing parameters used during LENS low and high power fabrications.

	Low power	High power
Laser power (W)	330	780
Powder feed rate (g/min)	1.0	2.0
Layer thickness (mm)	0.3	0.4
Hatch spacing (mm)	0.5	1.0
Deposition speed (m/min)	0.6	0.8

For each processing condition, a duplicate set of depositions was manufactured and heat treated (post-LENS annealing) at 1033 K +/- 4 K (760°C +/- 4°C) for 1 hour in vacuum, followed by air cool. Mill-annealed (wrought) Ti-Al-4V plates were used as substrate materials, on which near-net-shaped rectangular LENS depositions were built.

2.2. Metallographic preparation, microhardness measurements, and mechanical testing

LENS depositions were fabricated into near-net-shaped geometries, Figs. 3(a-c), designed for convenient extraction of metallographic (M) and mechanical testing specimens, while maintaining a minimum amount of material removal, Figs. 3(d-f).
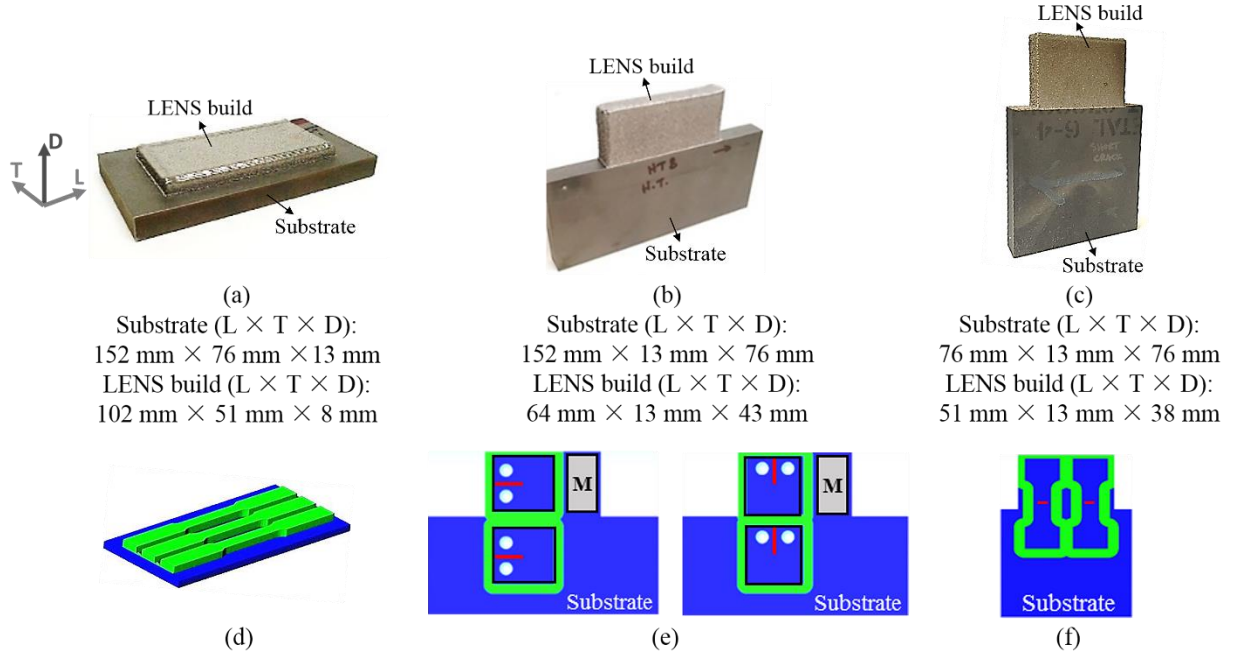
Fig. 3. Near-net-shaped LENS depositions designed for (a) tensile testing, (b) long fatigue crack growth testing, and (c) microstructurally-small fatigue crack growth testing; (d-f) layout of the specimens extracted for metallography (M) and mechanical testing.

Metallographic specimens were mounted in bakelite and polished using diamond suspensions. Samples were then etched using Kroll's reagent (2% HF, 6% HNO$_3$, and 92% DI H$_2$O). The microstructures were examined using a Nikon MA 200 Eclipse optical microscope with Element-D image analysis software. Vickers microhardness values were measured using a Shimadzu HMV-200 machine. A load of 1.96 N over 10 seconds was applied for each indentation.

Rectangular tensile specimens were machined per ASTM E8-15a, with a gage length of 25 mm, a gage cross-section of 6.4 mm × 5.0 mm and a grip cross-section of 9.5 mm × 5.0 mm. Tensile tests were conducted at room temperature, using an Instron universal testing frame, at a strain rate of 1.3 mm/min.

Long fatigue crack growth experiments were performed in both horizontal and vertical directions, as shown in Fig. 3(e). Compact tension specimens, Fig. 4(a), were machined per ASTM E647-15, with a specimen width (w) of 32 mm. Initial notch length (a_n) and specimen thickness (B) were determined according to the following relationships:

$$a_n = 0.2w \tag{1}$$

$$\frac{w}{20} \le B \le \frac{w}{4} \tag{2}$$
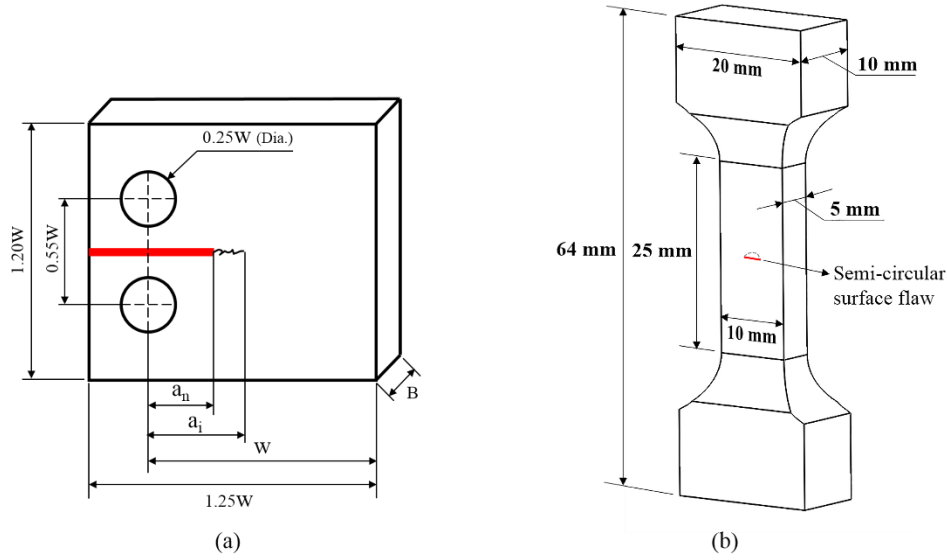
Fig. 4. (a) ASTM E647 standardized compact tension specimen; (b) Surface flaw tension specimen.

The overall specimen dimensions were 40 mm × 38 mm × 6 mm. The initial notch length was introduced by wire-cut electrical discharge machining (wire-EDM) with a wire thickness of 0.1 mm. Fatigue crack growth tests were conducted following ASTM E647-15, utilizing an Instron 8502 testing frame, which ensures a loading precision that is within ±2% of the target values for both P_{max} and ΔP, leading to a ±2% variation in ΔK, and a ±4% to ±10% variation in da/dN. Crack lengths during testing were determined by the compliance technique, using an MTS clip gage with a precision of ±0.01%. In addition, visual crack length measurements of ±0.0005 mm for initial and subsequent crack length were performed, and the compliance data were fitted to these measurements.

Long fatigue crack growth tests at constant stress ratio R=0.1 were performed for all conditions in horizontal and vertical directions, as shown in Fig. 3(e). Tests at R=0.8 were also performed for all conditions in the horizontal direction. The tests were run under K-control at a cyclic frequency of 20 Hz in order to generate data in Regions I and II, according to the following equations:

$$\Delta K = \Delta K_i \times e^{c(a-a_i)} \tag{3}$$

where c is the K-gradient, and has the following expression:

$$c = \frac{1}{K} \times \frac{dK}{da} \tag{4}$$

A K-gradient (c) of -0.2/mm was used to generate data in Region I and to determine the crack growth threshold value, ΔK_{th}. A K-gradient (c) of +0.2/mm was used for the increasing K part of the test to generate data in Region II. Region III of fast crack growth data were collected by running test at constant load and a lower cyclic frequency of 5 Hz. Physically-small fatigue crack growth data were predicted by removing the effects of crack closure from long fatigue crack growth data, using the Adjusted Compliance Ratio (ACR) technique [25,31].

Microstructurally-small fatigue crack growth testing was conducted using a surface flaw tension specimen, as illustrated in Fig. 3(f), and the specimen geometry is shown in Fig. 4(b). A semicircular surface flaw was introduced by wire-EDM, using a wire thickness of 0.025 mm. The initial notch size was 100 μm in radius. The microstructurally-small fatigue crack growth test was run under load control at constant stress ratio R=0.1 and a cyclic frequency of 20 Hz. The direct current potential drop (DCPD) method was used to

determine crack length. All fatigue crack growth testing were performed at room temperature in lab air, with a relative humidity of 20-50%.

Long and small fatigue crack growth data were collected, analyzed using FTA's (Fracture Technology Associates) Automated Fatigue Crack Growth Analysis software, and then plotted in Grapher[TM]. To establish the long fatigue crack growth damage mechanisms, one half of the fractured compact tension specimen was vertically sectioned through the middle of the thickness and metallographically prepared for two-dimensional examination of the crack path (side view). The other half was used for examination of the fracture surfaces (top view), using a JEOL-7000F scanning electron microscope (SEM). This process was performed on all tested long fatigue crack growth specimens. The fracture surface of the surface flaw tension specimen was also examined under SEM.

3. Results and discussion

3.1. Microstructure characterization and tensile properties

Cross-sectional panoramas of low and high power fabricated LENS Ti-Al-4V builds (4 cm tall) are shown in Figs. 5(a,b). The panoramas were taken in as-fabricated condition. Columnar prior β grains oriented parallel to the deposition direction (D) are observed in both cases as a result of heat extraction from the substrate during solidification. Heat affected zones (HAZ) are observed between LENS layers, referred to as micro-HAZ, Figs. 5(c,d), due to partial remelting of previous layers upon subsequent depositions, leading to a "banded" microstructure. Macro-HAZ are also observed at the substrate-LENS interfaces, Figs. 5(g,h), due to partial melting of the substrate. Compared to the low power built Ti-6Al-4V, high power built materials yield coarser columnar grains, as well as thicker layer bands and macro-HAZ. In addition, a single gas pore is observed in both processing conditions, located near the macro-HAZ. The size of the pore is bigger in high power LENS depositions, highlighted by the circles in Figs. 5(g,h). Previous studies demonstrated that the single gas pore observed did not affect the bonding at the interfaces [32].

At high magnification, the microstructure of low power as-fabricated Ti-6Al-4V appears martensitic with very fine acicular α' phase, Fig. 5(e). High power as-fabricated Ti-6Al-4V shows regions of α colonies as well as regions of acicular α' phase, Fig. 5(f), leading to a mixed microstructure of α+α' in prior β matrix. In addition, the formation of continuous α layers (1-2 μm thick) at β grain boundaries are observed in the high power case, but not in low power case, indicating slower cooling rates during high power fabrication. After heat treatment, the martensitic α' phase in the as-fabricated condition changes to a fine α+β microstructure by forming β phase as a continuous layer between martensitic plates [33]. This change in microstructure could not be observed using the optical microscope, but evidences were found in tensile and microhardness data. Within the micro-HAZ, microstructure coarsening was observed in both cases as a result of partial remelting of previous layers. The transitioning from fine α'/α within the layers to coarser α'/α within the micro-HAZ are shown in Figs. 6(a,b). In addition, the α' thickness was measured to be less than 0.73 μm within one layer, and ~0.86 μm within the micro-HAZ for low power as-fabricated Ti-6Al-4V. For high power as-fabricated Ti-6Al-4V, the α lath thickness was ~0.79 μm within one layer, and ~1.06 μm within the micro-HAZ, Fig. 7. Substrate material is a mill-annealed Ti-6Al-4V plate, with a typical microstructure of equiaxed α in β matrix, Fig. 6(c).
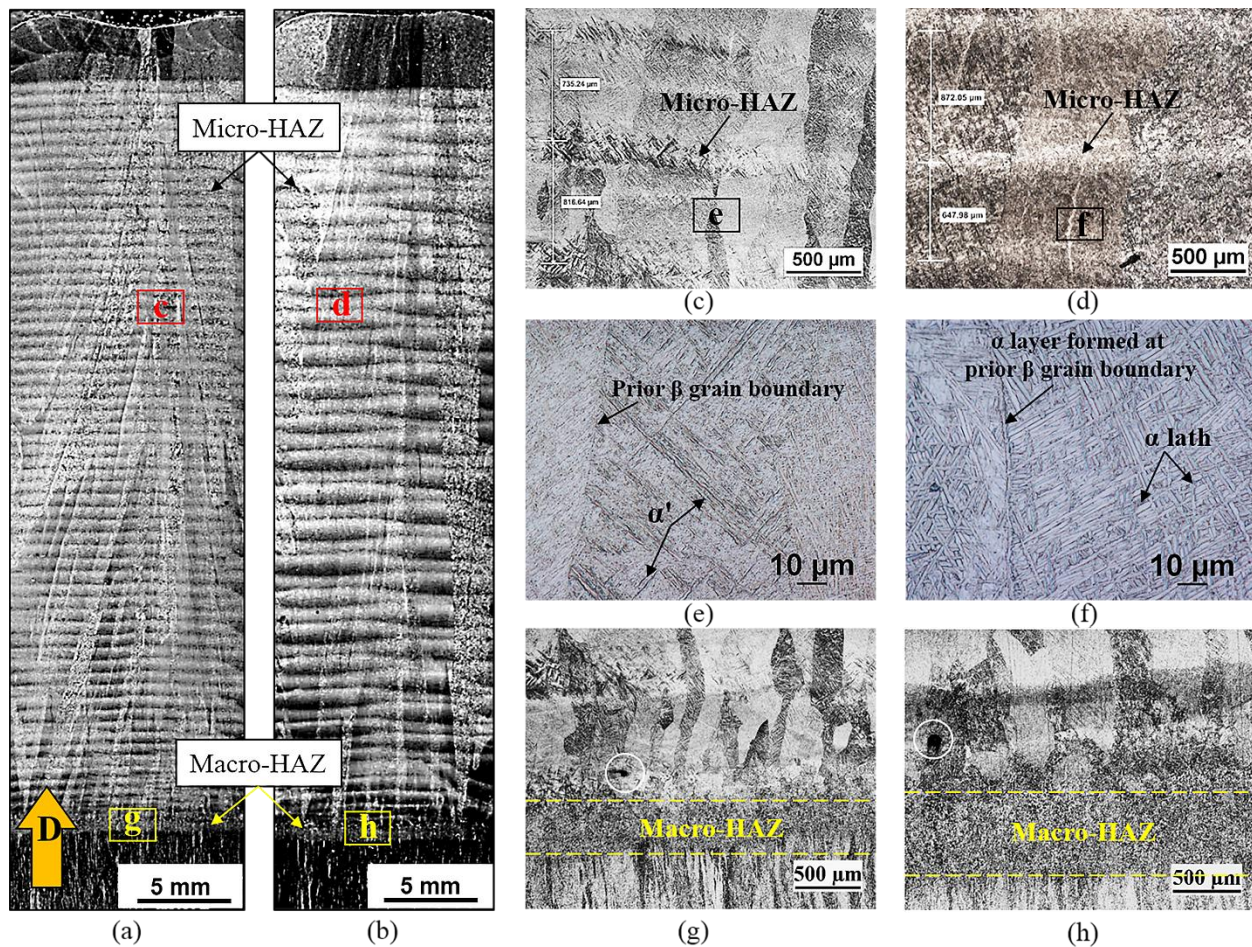
Fig. 5. (a,b) Microstructural panoramas showing the cross-sections of LENS low and high power builds; (c,d) micro-HAZ in low and high power builds; (e) martensitic microstructure in low power as-fabricated Ti-6Al-4V and (f) mixed microstructure of acicular α' and lamellar α+β in high power as-fabricated Ti-6Al-4V; (g,h) macro-HAZ and gas pores generated during low and high power fabrication.
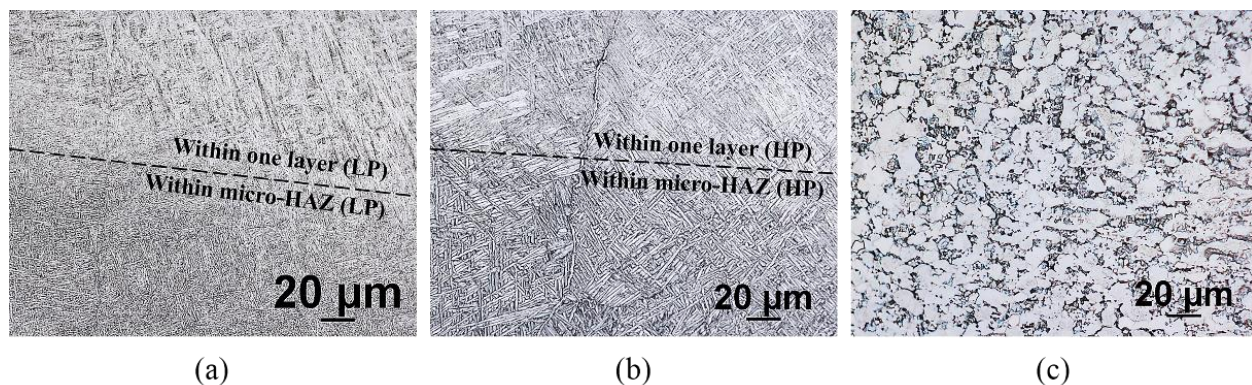
Fig. 6. Coarsening of α'/α in micro-HAZ in (a) low power and (b) high power fabricated Ti-6Al-4V; (c) mill-annealed Ti-6Al-4V substrate.

7

(a) α' thickness: <0.73 μm (0.11 μm SD)

(b) α lath thickness: 0.79 μm (0.16 μm SD)

(c) α' thickness: 0.86 μm (0.22 μm SD)

(d) α lath thickness: 1.06 μm (0.21 μm SD)
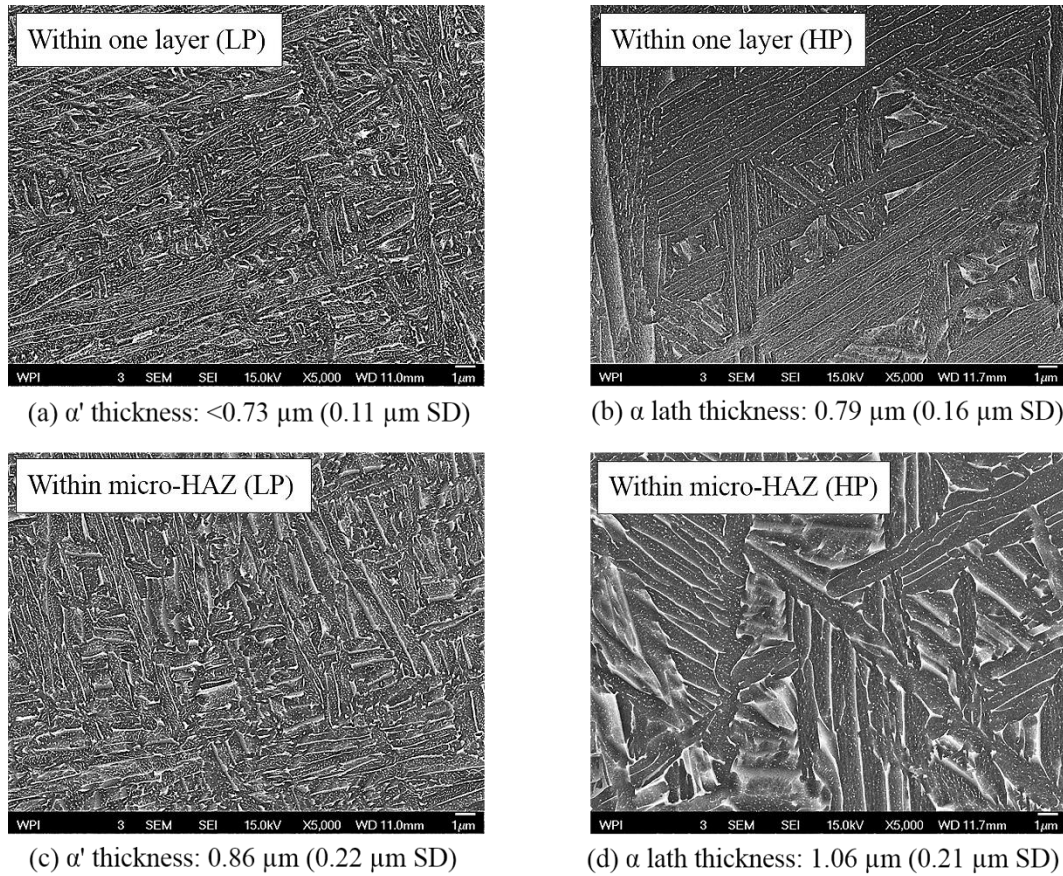
Fig. 7. Finer α'/α within one layer, and coarser α'/α within micro-HAZ between layers in (a,c) low power and (b,d) high power fabricated Ti-6Al-4V.

The room temperature tensile data, and microhardness measurements for all LENS Ti-6Al-4V conditions are summarized in Table 2, and compared to mill-annealed Ti-6Al-4V. LENS low power as-fabricated Ti-6Al-4V has the highest tensile strength and microhardness, but the lowest ductility, due to its martensitic microstructure. High power as-fabricated Ti-6Al-4V contains a lower fraction of martensitic α', resulting in an increase in ductility, as well as a decrease in tensile strength and microhardness. After heat treatment, a significant increase in ductility is achieved in both low power (125% increase) and high power (43% increase) cases. It was observed that, conventional mill-annealed Ti-6Al-4V (substrate) yields much higher ductility but lower strength than LENS Ti-6Al-4V.

Table 2
Room temperature tensile properties (0.2% offset yield strength, ultimate tensile strength, and elongation at failure) and microhardness measurements of LENS and mill-annealed Ti-6Al-4V.

	LPAF	LPHT	HPAF	HPHT	Substrate
YS (MPa)	1005	1000	990	991	970
UTS (MPa)	1103	1073	1042	1044	1030
%EL	4	9	7	10	16
Microhardness (HV)	360	330	325	320	320

LP – low power, HP – high power, AF – as-fabricated, HT – heat-treated

3.2. Long and physically-small fatigue crack growth behavior at low stress ratio R=0.1

The long fatigue crack growth data of LENS and mill-annealed (substrate) Ti-6Al-4V are summarized in Fig. 8(a) for the horizontal propagation cases, and Fig. 8(b) for the vertical propagation cases. In both propagation directions, LENS Ti-6Al-4V yields lower threshold values (ΔK_{th}) and faster fatigue crack growth rates in Region II of stable crack growth than mill-annealed Ti-6Al-4V. In Region III, slower fatigue crack growth rates were achieved in LENS Ti-6Al-4V, leading to higher fracture toughness values (ΔK_{FT}). Comparing the fatigue crack growth behavior of LENS Ti-6Al-4V under various conditions, low power as-fabricated Ti-6Al-4V shows lower ΔK_{th} than high power as-fabricated material. After heat treatment, a slight increase in ΔK_{th} was observed in the low power case but not in the high power case. This could be attributed to a larger fraction of martensitic α' phase in low power as-fabricated Ti-6Al-4V, which decomposes into α+β lamellae during heat treatment. Corresponding ΔK_{th} and ΔK_{FT} values are listed in Table 3. Paris constants, C and m values, can be obtained using FTA's Automated Fatigue Crack Growth Analysis software by manually setting upper and lower da/dN limits. The calculated values are also summarized in Table 3 (the unit of C is derived as $\dfrac{m}{cycle \times (MPa\sqrt{m})^m}$).

Fig. 8. Long fatigue crack growth behavior of LENS and mill-annealed Ti-6Al-4V at R=0.1 in (a) horizontal and (b) vertical propagation directions.

Table 3
Long fatigue crack growth threshold and fracture toughness values, and C and m constants in Pairs Region II for R=0.1 (H – Horizontal, V – Vertical).

	LPAF		LPHT		HPAF		HPHT		Substrate	
	H	V	H	V	H	V	H	V	H	V
ΔK_{th} (MPa√m)	2.6	2.6	2.9	2.9	3.4	3.5	3.2	3.6	4.4	4.4
ΔK_{FT} (MPa√m)	51.9	51.1	53.0	46.7	52.8	48.0	47.8	49.1	39.4	43.0
C	1.7E-11	2.7E-12	4.4E-12	1.4E-12	5.6E-13	2.4E-12	6.6E-13	9.0E-13	5.2E-14	2.1E-14
m	3.2	3.7	3.7	4.0	4.4	3.9	4.3	4.2	5.0	5.4

Physically-small fatigue crack growth data (obtained using ACR closure correction of long fatigue crack growth data [25, 31]) of LENS and mill-annealed Ti-6Al-4V are shown in Fig. 9, for the horizontal and vertical propagation cases. It was observed that after closure correction, the Region I fatigue crack growth data for all materials and conditions shift to lower ΔK values, and thus lead to smaller ΔK_{th} values. Compared to LENS Ti-6Al-4V, a more significant change is seen in mill-annealed Ti-6Al-4V due to the much coarser microstructure, which generates more roughness induced closure effects. In LENS Ti-Al-4V,

more threshold shifting is noticed in the vertical propagation cases, as seen by comparing ΔK_{th} values in Table 4 with those in Table 3. This phenomenon is related to the influence of columnar β grains and layer boundaries during vertical crack propagation, and is further discussed in section 3.4.1.
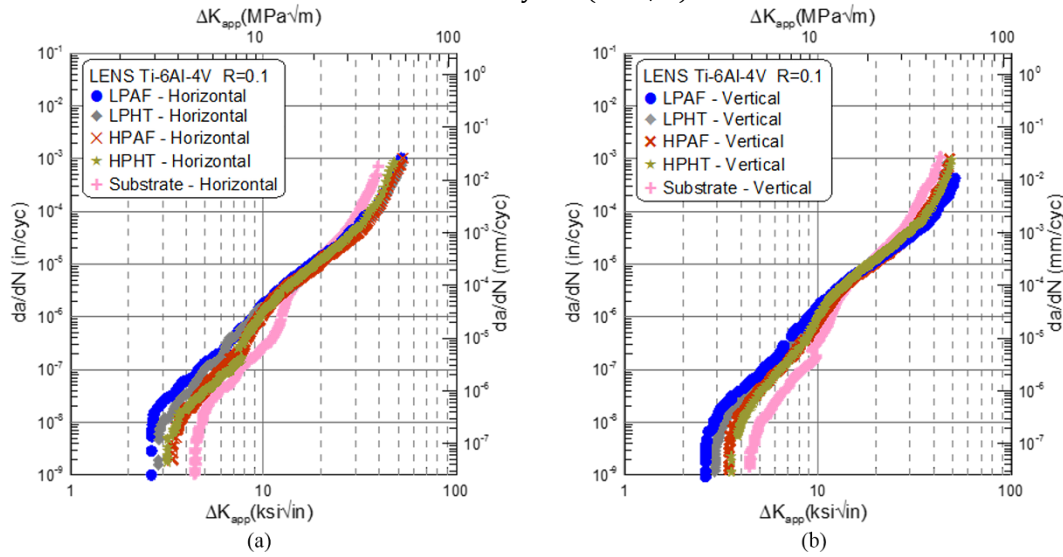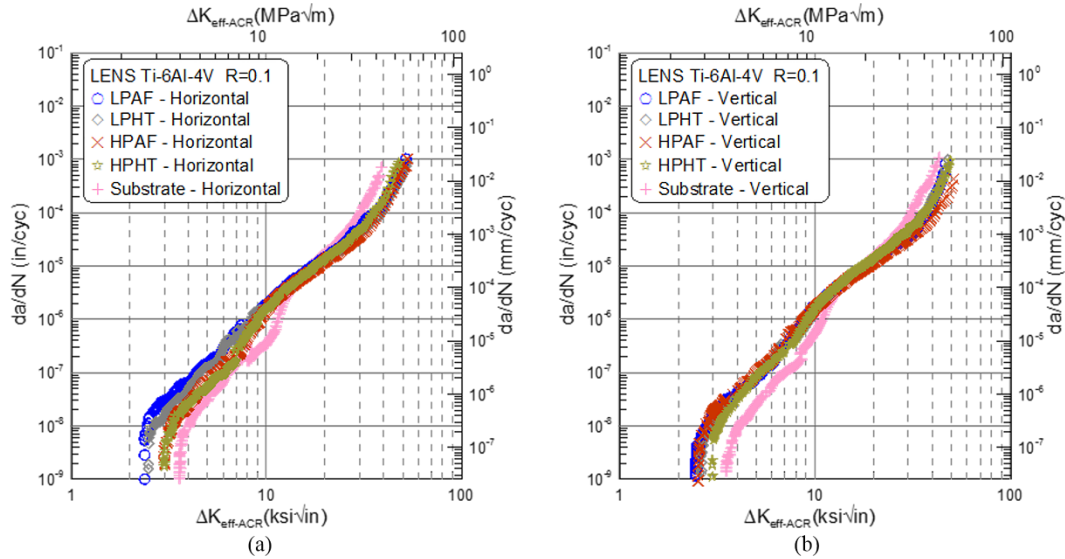

Fig. 9. Physically-small fatigue crack growth behavior of LENS and mill-annealed Ti-6Al-4V at R=0.1 in (a) horizontal and (b) vertical propagation directions.

Table 4
Physically-small fatigue crack growth threshold values, and C and m constants in Pairs Region II for R=0.1 (H – Horizontal, V – Vertical).

	LPAF		LPHT		HPAF		HPHT		Substrate	
	H	V	H	V	H	V	H	V	H	V
ΔK_{th} (MPa√m)	2.4	2.5	2.5	2.4	3.00	2.6	3.00	3.0	3.6	3.5
C	6.2E-12	4.8E-12	6.3E-12	2.6E-12	1.1E-12	2.9E-12	6.5E-13	3.4E-12	3.4E-13	1.8E-13
m	3.6	3.6	3.6	3.9	4.2	3.9	4.4	3.8	4.4	4.7

3.3. Long fatigue crack growth behavior at high stress ratio R=0.8

Long fatigue crack growth data obtained from higher stress ratio (R=0.8) tests are plotted in Fig. 10 for LENS Ti-6Al-4V in the as-fabricated and heat treated conditions. Compared to the physically-small crack growth data shown in Fig. 8(a), the fatigue crack growth curves shift towards even lower ΔK values for the high stress ratio case. This phenomenon is explained by the second order K_{max} effect, which is introduced during high stress ratio tests, when the K_{max} level increases significantly to achieve the desired crack propagation rates. It is also important to note that at the high stress ratio, ΔK_{th} differences between low power and high power fabricated materials still exist for both as-fabricated and heat treated conditions, indicating that these differences are intrinsic to the material and induced by microstructural variations. The corresponding threshold values are listed in Table 5.
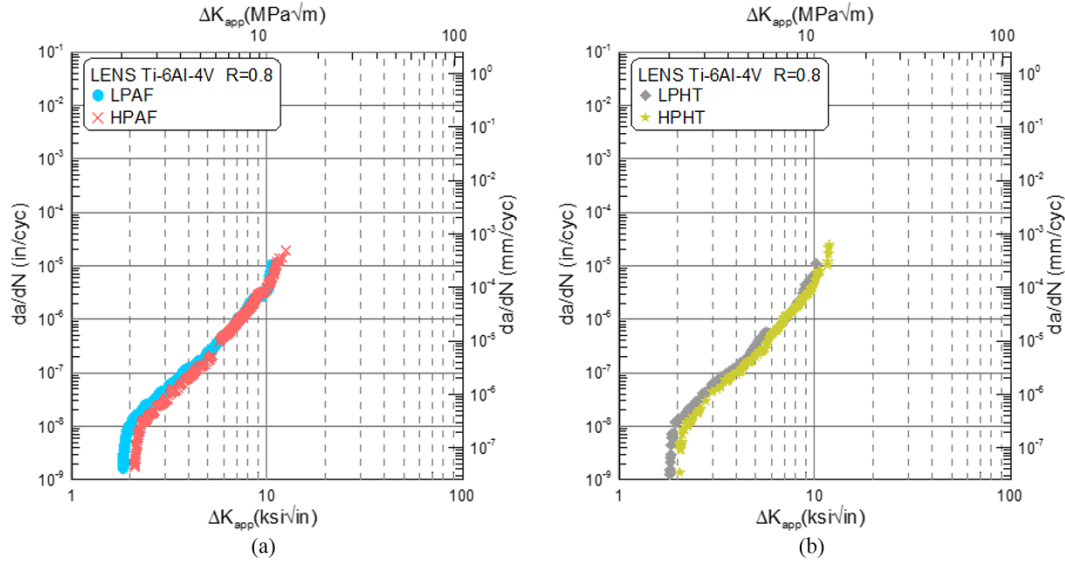
Fig. 10. Long fatigue crack growth behavior of LENS Ti-6Al-4V for R=0.8 in (a) as-fabricated and (b) heat treated conditions.

Table 5
Long fatigue crack growth threshold values, and C and m constants in Pairs Region II for for R=0.8.

	LPAF	LPHT	HPAF	HPHT
ΔK_{th} (MPa√m)	1.8	1.8	2.1	2.1
C	1.5E-11	1.6E-11	6.0E-12	6.3E-12
m	3.6	3.6	4.0	4.1

3.4. Long fatigue crack growth mechanisms

The fatigue crack growth behavior of a material is largely related to its characteristic microstructural features. The unique thermal history during LENS fabrication yields directional microstructural features including columnar β grains and layer boundaries, which are large in scale (range from tens to hundreds of microns). The fast cooling rates on the other hand, produce very fine α morphologies (less than 2 µm). All of these microstructural features are considered in the following discussions.

3.4.1. Effects of columnar β grains and layer bands

The panoramic fatigue crack growth path side profiles for the horizontal and vertical propagation directions are shown in Figs. 11(a,b). Horizontal propagation indicates a growth direction perpendicular to the columnar grains and parallel to the layer boundaries, as illustrated in Fig. 12. The side profile, Fig. 11(a), shows limited crack interaction with columnar grain boundaries as the crack grows through smoothly upon encountering β grain boundaries. During vertical propagation, the crack growth direction is parallel to the columnar grains and perpendicular to the layer boundaries, Fig. 12. Clear crack interaction with the layer boundaries were observed at various crack growth stages, leading to a serrated fracture surface, as shown in Fig. 11(b). This interaction is also seen on the fracture surface of vertical propagation, Fig. 13(d), where parallel "lines" are seen as a result of crack's interaction with layer boundaries. This phenomenon, however, is not observed on the horizontal propagation fracture surface, Fig. 13(c). In addition, crack interactions with columnar β grain boundaries are also easily identified on the fracture surface, Figs. 13(d,e,f). The crack interaction with both layer boundaries and columnar β grain boundaries contribute to a rougher fracture surface, and lead to more roughness induced closure effects during vertical crack propagation.
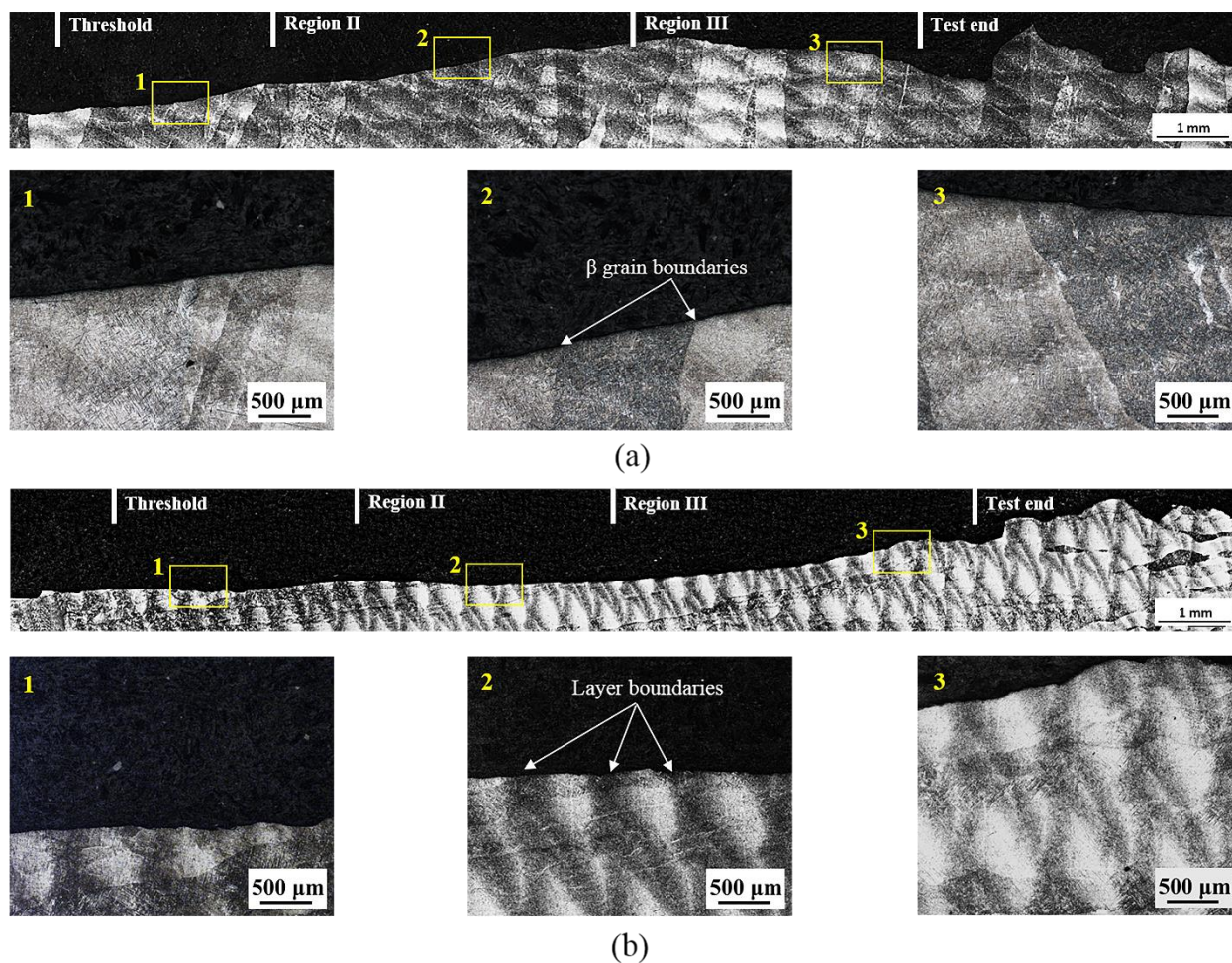
Fig. 11. (a) Horizontal and (b) vertical fatigue crack growth path side profiles: panoramic views and zoom-ins from three fatigue crack growth regions.
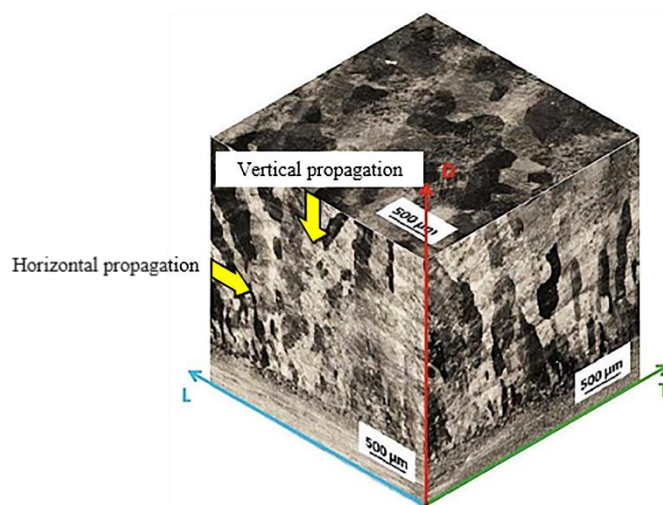

Fig. 12. 3D illustration of horizontal and vertical fatigue crack propagation.
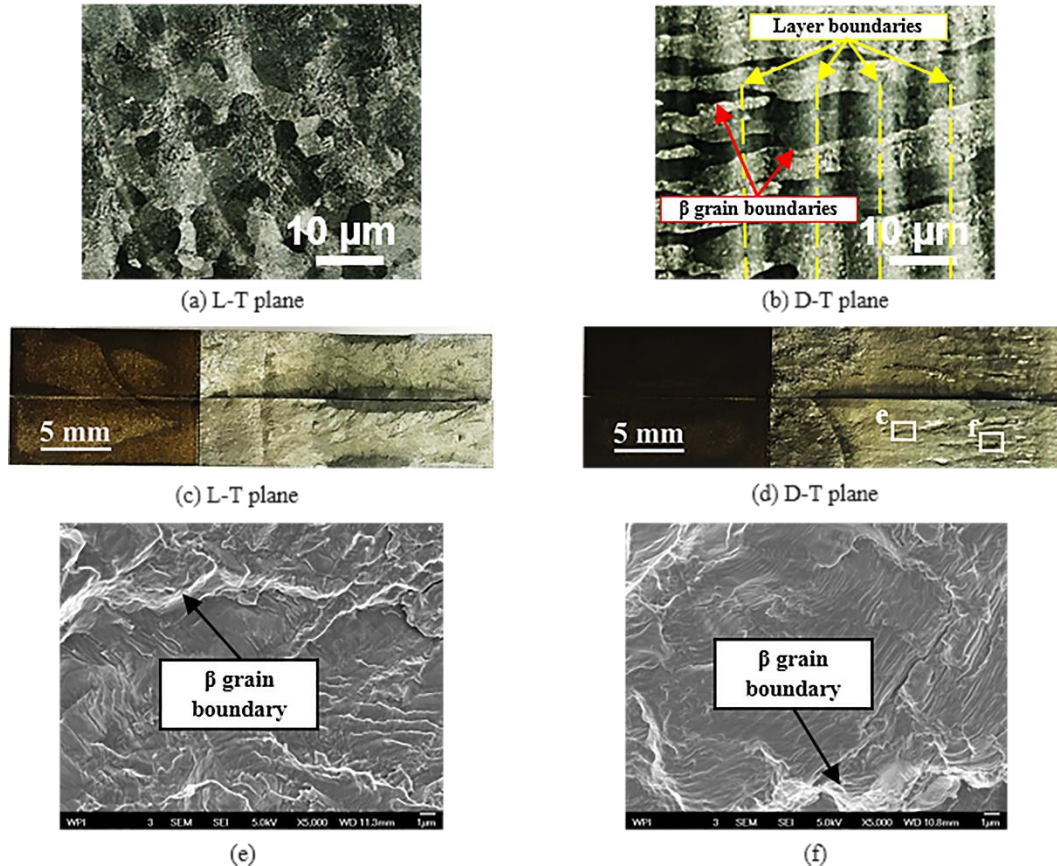
Fig. 13. Microstructure underneath the fracture surfaces and optical observations of the fracture surfaces for (a,c) horizontal and (b,d) vertical propagation directions; SEM fractographs showing crack interaction with prior β grain boundaries during vertical propagation at: (e) ΔK~11 MPa√m (Region II) and (f) ΔK~36 MPa√m (Region III).

3.4.2. Influence of α morphology

In titanium alloys, α morphology plays an important role in the fatigue crack growth behavior of the material. During LENS fabrication, pre-alloyed Ti-6Al-4V powder is fully melted, leading to an "as-cast", lamellar microstructure upon solidification. Cooling rates during LENS are commonly fast, resulting in very fine α lath morphology (which massively exist in high power as-fabricated Ti-6Al-4V), and in some cases, martensitic α' with an acicular morphology (typically found in low power as-fabricated Ti-6Al-4V). Mill-annealed Ti-6Al-4V contains an equiaxed α morphology, which forms during recrystallization following hot working [33]. High magnification crack path side profiles at certain ΔK levels representing the threshold, Region II, and Region III of fatigue crack growth, are shown in Fig. 14 for LENS low power and high power Ti-6Al-4V in as-fabricated condition, as well as for mill-annealed Ti-6Al-4V.

From these side profiles, crack interaction with the lamellar microstructure was observed at high magnification at all ΔK levels. As shown in Figs. 14(a-c), for low power as-fabricated Ti-6Al-4V, crack interaction with acicular α' was identified. In Figs. 14(d-f), for high power as-fabricated Ti-6Al-4V, crack interactions with slightly coarser α+β lamellae and α' phase were observed. It is also observed that prior β grain boundaries did not affect the crack propagation during horizontal propagation, as crack grows smoothly across when intersecting a grain boundary, Fig. 14(e). Similar crack interaction with the lamellar microstructure was observed during vertical propagation, and are thus not repeated here. The crack propagation mechanisms in mill-annealed Ti-6Al-4V were also investigated, Figs. 14(g-i). Crack interaction with equiaxed α is primarily found near threshold. With increasing crack tip driving force (ΔK),

the plastic zone samples more material ahead of the crack tip, and the crack shows increased interactions with the β matrix in Region II. Finally, at high ΔK levels, crack growth is mainly through the β matrix.
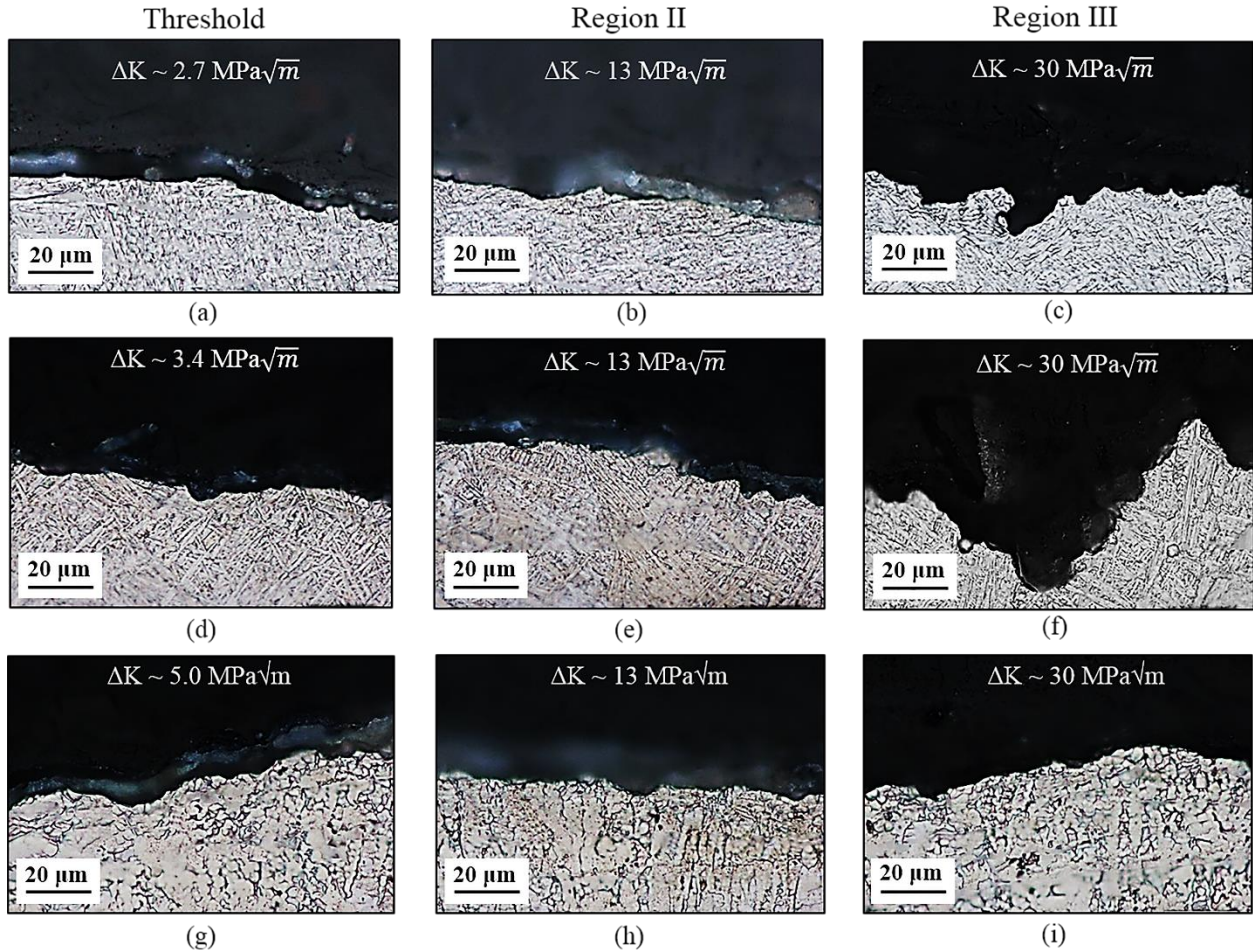

Fig. 14. Fatigue crack interactions with various α morphologies at different ΔK levels in (a-c) low power and (d-f) high power as-fabricated Ti-6Al-4V; (g-i) mill-annealed Ti-6Al-4V.

Since the crack propagation mechanism in LENS Ti-6Al-4V is primarily through the lamellar microstructure, the differences in the fatigue crack growth thresholds are explained by the size difference between acicular α' and α lath. During low power fabrication, fast cooling rates result in martensitic microstructure (acicular α' morphology) with an average width of between 0.7-0.9 μm. In comparison, the higher energy input during high power fabrication yields slower cooling rates, and yields a mixed microstructure of coarser α+β lamellae with an average lath thickness between 0.8-1.1 μm. The finer microstructure in low power fabricated Ti-6Al-4V is unfavorable and results in a lower fatigue crack growth threshold. During post-LENS annealing, α' transforms into fine α+β microstructure, but retained the size difference between low and high power fabricated Ti-6Al-4V, thus the difference in ΔK_{th} is still observed.

Representative SEM fractographs are taken for low and high power LENS and mill-annealed Ti-6Al-4V at corresponding ΔK values, as shown in Fig. 15. For all materials, fracture surfaces revealed facets in the near threshold regime, Figs. 15(a,d,g), resulting from the crystallographic mode of crack propagation. In the Paris regime, Figs. 15(b,e,h), fatigue striations are present. Their values were measured in Element-D image analysis software, and were represented by the averaged quotients of the length of lines and the number of intercepting striations. The finer striation spacing in mill-annealed Ti-6Al-4V indicates a slower propagation rate. Whereas, in Region III, Figs. 15(c,f,i), faster propagation rate can be inferred in mill-

annealed Ti-6Al-4V from the coarser striation spacing. These observations are in good agreement with the fatigue crack growth data shown in Fig. 8.

Threshold | Region II | Region III

(a)

(b)

Average striation spacing: 0.31 μm
(SD: 0.03 μm)

(c)

Average striation spacing: 0.89 μm
(SD: 0.01 μm)

(d)

(e)

Average striation spacing: 0.25 μm
(SD: 0.05 μm)

(f)

Average striation spacing: 0.47 μm
(SD: 0.04 μm)

(g)

(h)

Average striation spacing: 0.24 μm
(SD: 0.01 μm)

(i)

Average striation spacing: 1.22 μm
(SD: 0.02 μm)
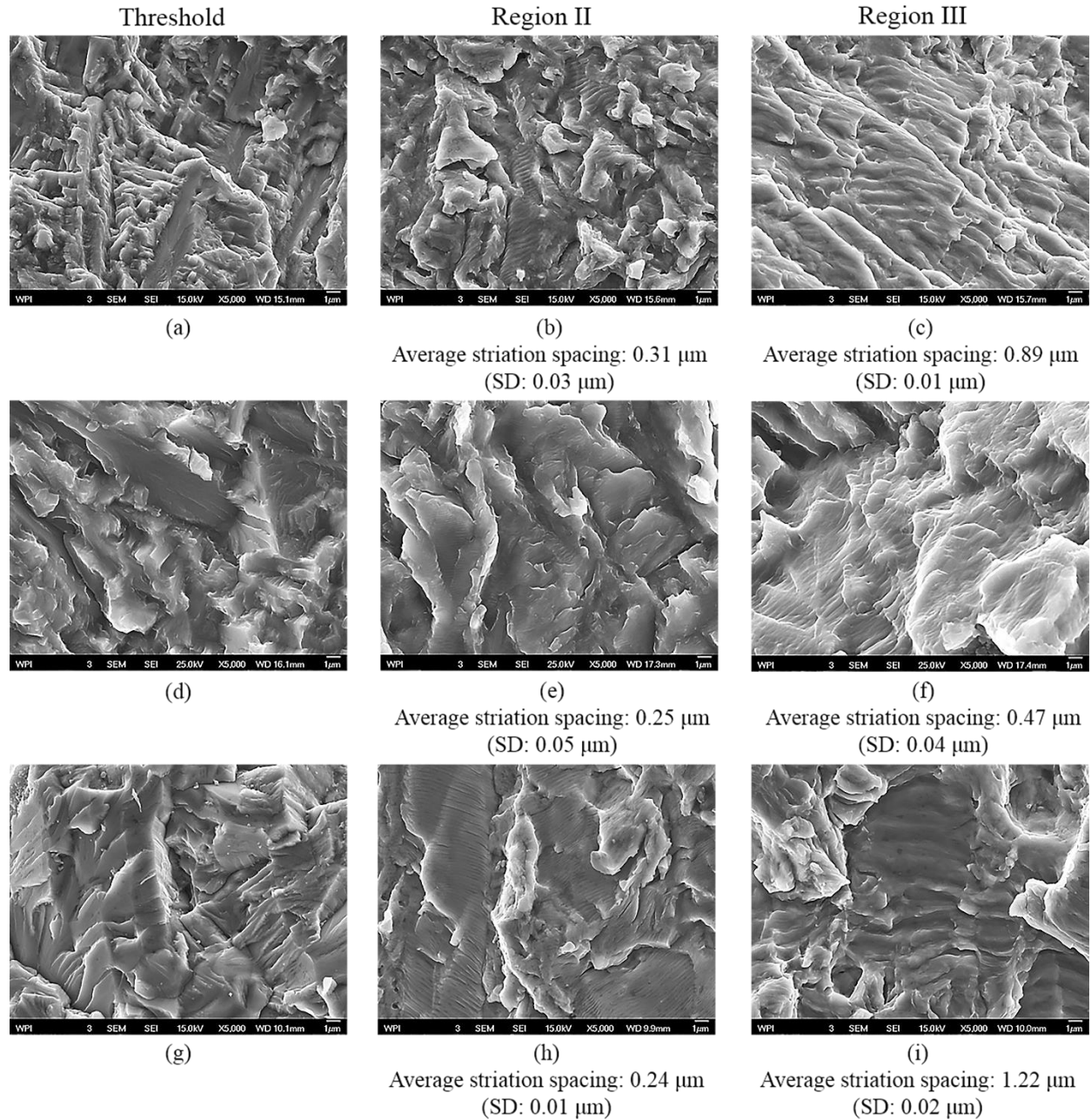
Fig. 15. Fractographs taken at ΔK levels corresponding to those in Fig. 14 for: (a-c) low power; (d-f) high power as-fabricated Ti-6Al-4V (horizontal direction); (g-i) mill-annealed Ti-6Al-4V.

3.5. Microstructurally-small fatigue crack growth behavior and mechanism

Microstructurally-small fatigue crack growth data for LENS low power as-fabricated Ti-6Al-4V is plotted together with the corresponding long and physically-small data in Fig. 16(a). The acceleration/retardation behavior of the small crack could be related to its interaction with local microstructural characteristics at the meso-scale in early stages of growth. SEM fractographs, Figs. 16(b,c), were taken at the specific ΔK values where the retardation the in fatigue crack growth rate occurred, and

15

similar interactions of the crack with columnar β grain boundary were observed at both locations. This phenomenon is known as the blocking effect of grain boundaries, which is considered to result from the difference in orientation between the grain containing the crack and the adjacent grain, as well as the absence of atoms and presence of strain. This observation is valuable considering that this blocking effect increases with finer grain size. In other words, if the columnar grain size can be minimized, it is possible to improve the microstructurally-small fatigue crack growth resistance. The compiled data also confirm the significantly lower threshold values for small cracks compared to long cracks, indicating the importance of taking small fatigue crack growth data into consideration for structural applications.
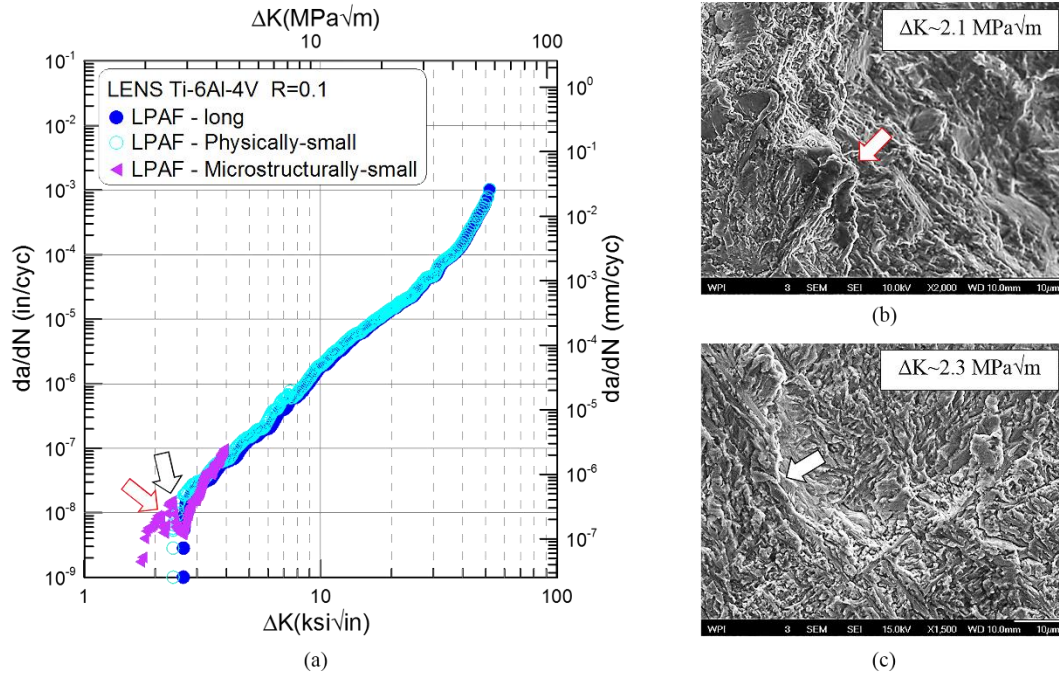

Fig. 16. (a) microstructurally-small fatigue crack growth data compiled with physically-small and long fatigue crack growth data; crack interaction with local microstructural features at (b) ΔK ~ 2.1 MPa√m, and (c) ΔK ~ 2.3 MPa√m.

4. Conclusions

In this study, the fatigue crack growth behavior of Ti-6Al-4V fabricated by LENS was investigated and compared to that of the conventional mill-annealed Ti-6Al-4V, taking into account the influence of processing parameters, post-LENS heat treatment, and crack propagation directions. The fatigue crack growth mechanisms for both long and small cracks were also established. A summary of the important findings from this study is provided here.

- The lamellar microstructures in LENS fabricated Ti-6Al-4V yield lower threshold but higher fracture toughness than conventional mill-annealed Ti-6Al-4V which contains equiaxed α phase in β matrix.
- The α phase morphology is the controlling factor of the fatigue crack growth behavior in LENS Ti-6Al-4V. Low power fabrication yields martensitic α' which has an unfavorable acicular morphology. High power fabrication produces coarser α morphology, and results in slightly higher fatigue crack growth thresholds and lower Region II fatigue crack growth rates.
- Post-LENS annealing applied in this study decomposes α' martensite, thus increases the material's ductility. Whereas, the temperature and time applied are not enough to alter the size and

morphology of α, and do not eliminate the differences in the fatigue crack growth thresholds between low and high power fabricated Ti-6Al-4V.

- Interferences from the layer and grain boundaries are observed only when the fatigue crack growth direction is parallel to the columnar grains, and perpendicular to the layer bands (i.e., during vertical propagation). These interferences lead to more roughness-induced closure effects.
- Acceleration and retardation in fatigue crack growth rates are observed during microstructurally-small fatigue crack propagation due to the blocking effects at prior β grain boundaries. This finding indicates that the microstructurally-small fatigue crack growth resistance may be improved by grain refinement.
- The fatigue crack growth threshold values of small cracks are significantly lower than those of long and physically small cracks, indicating the importance of incorporating small fatigue crack growth data into design, and establishing the small fatigue crack growth mechanisms at the microstructural scale.

Acknowledgement

References

[1] T. Wohlers, Wohlers Report 2013, Wohlers Associates, Inc., Fort Collins, Colorado, USA, 2013.

[2] M.L. Griffith, M.T. Ensz, J.D. Puskar, C.V. Robino, J.A. Brooks, J.A. Philliber, J.E. Smugeresky and W.H. Hofmeister, Understanding the Microstructure and Properties of Components Fabricated by Laser Engineered Net Shaping (LENS), MRS Proceedings, vol. 625, 2000. Doi: 10.1557/PROC-625-9.

[3] M.L. Griffith, D.M. Keicher, and C.L. Atwood, Free form fabrication of metallic components using laser engineered net shaping (LENS), Proceedings of the Solid Freeform Fabrication Symposium. Austin, TX, 1996.

[4] X. Wu, J. Liang, J. Mei, C. Mitchell, P.S. Goodwin, and W. Voice, Microstructures of laser-deposited Ti–6Al–4V, Materials & Design, vol. 25(2), pp. 137–144, 2004.

[5] F. Wang, J. Mei, and X. Wu, Microstructure study of direct laser fabricated Ti alloys using powder and wire, Applied Surface Science, vol. 253(3), pp. 1424–1430, 2006.

[6] X. Wu, R. Sharman, J. Mei, and W. Voice, Microstructure and properties of a laser fabricated burn-resistant Ti alloy, Materials and Design, vol. 25, pp. 103–109, 2004.

[7] X. Wu, and J. Mei, Near net shape manufacturing of components using direct laser fabrication technology, Journal of Materials Processing Technology, vol. 135, pp. 266–270, 2003.

[8] X. Wu, R. Sharman, J. Mei , and W. Voice, Direct laser fabrication and microstructure of a burn-resistant Ti alloy, Materials and Design, vol. 23, pp. 239-247, 2002.

[9] S.M. Kelly and S.L. Kampe, Microstructural Evolution in Laser-Deposited Multilayer Ti-6Al-4V Builds: Part I. Microstructural Characterization, Metallurgical and Materials Transactions A, vol. 35(6), pp. 1861-1867, 2004.

[10] S.M. Kelly and S.L. Kampe, Microstructural Evolution in Laser-Deposited Multilayer Ti-6Al-4V Builds: Part II. Thermal Modeling Metallurgical and Materials Transactions A, vol. 35(6), pp. 1869-1879, 2004.

[11] E. Amsterdam, and G.A. Kool, High cycle fatigue of laser beam deposited Ti-6Al-4V and Inconel 718, ICAF Bridging the gap between theory and operational practices, pp. 1261-1274, 2009. DOI: 10.1007/978-90-481-2746-7_71.

[12] P.A. Kobryn, and S.L. Semiatin, Mechanical Properties of laser-deposited Ti-6Al-4V, Edited by D.L. Bourell, J.J. Beaman, R.H. Crawford, H.L. Marcus, L. Wood, J.W. Barlow, proceedings of the SFF conference, Austin, Texas, USA, pp. 179-186, 2001.

[13] A.W. Prabhu, T. Vincent, A. Chaudhary, W. Zhang, and S.S. Babu, Effect of microstructure and defects on fatigue behaviour of directed energy deposited Ti–6Al–4V, Science and Technology of Welding and Joining vol. 20(8), pp. 659-669, 2015.

[14] P. Ganesha, R. Kaul, C.P. Paul, P. Tiwari, S.K. Rai, R.C. Prasad, and L.M. Kukreja, Fatigue and fracture toughness characteristics of laser rapid manufactured Inconel 625 structures, Materials Science and Engineering A, vol. 527(29-30), pp. 7490-7497, 2010.

[15] E. Brandl, U. Heckenberger, V. Holzinger, and D. Buchbinder, Additive manufactured AlSi10Mg samples using Selective Laser Melting (SLM): Microstructure, high cycle fatigue, and fracture behavior, Materials and Design, vol. 34, pp. 159–169, 2012.

[16] S. Leuders, A. Thöne, A. Riemer, T. Niendorf, T. Tröster, H.A. Richard, and H.J. Maier, On the mechanical behavior of titanium alloy TiAl6V4 manufactured by selective laser melting: Fatigue resistance and crack growth performance, International Journal of Fatigue, vol. 48, pp. 300–307, 2013.

[17] S.J. Li, L.E. Murr, X.Y. Cheng, Z.B. Zhang, Y.L. Hao, R. Yang, F. Medina, and R.B. Wicker, Compression fatigue behavior of Ti–6Al–4V mesh arrays fabricated by electron beam melting, Acta Materialia, vol. 60, pp. 793–802, 2012.

[18] L.E. Murr, S.A. Quinones, S.M. Gaytan, M.I. Lopez, A. Rodela, E.Y. Martinez, D.H. Hernandez, E. Martineza, F. Medina, and R.B. Wicker, Microstructure and mechanical behavior of Ti–6Al–4V produced by rapid-layer manufacturing, for biomedical applications, Journal of the Mechanical Behavior of Biomedical Materials, vol. 2(1), pp. 20–32, 2009.

[19] B. Gorny, T. Niendorf, J. Lackmann, M. Thoene, T. Troester, and H.J. Maier, In situ characterization of the deformation and failure behavior of non-stochastic porous structures processed by selective laser melting, Materials Science and Engineering A, vol. 528, pp. 7962–7967, 2011.

[20] P. Edwards, A. O'Conner and M. Ramulu, Electron Beam Additive Manufacturing of Titanium Components: Properties and Performance, Journal of Manufacturing Science and Engineering, vol. 135(6), 061016-1-061016-7, 2013. DOI: 10.1115/1.4025773.

[21] P. Edwards, and M. Ramulu, Fatigue performance evaluation of selective laser melted Ti–6Al–4V, Materials Science & Engineering A, vol. 598, pp. 327–337, 2014.

[22] S.K. Chan, M. Koike, R.L. Mason, and T. Okabe, Fatigue Life of Titanium Alloys Fabricated by Additive Layer Manufacturing Techniques for Dental Implants, Metallurgical and Materials Transactions A, vol. 44(2), pp. 1010-1022, 2013.

[23] F. Wang, Mechanical property study on rapid additive layer manufacture Hastelloy® X alloy by selective laser 15-21melting technology, The International Journal of Advanced Manufacturing Technology, vol. 58(5), pp. 545-551, 2012.

[24] J.P. Campbell, and R.O. Ritchie, Mixed-mode, high-cycle fatigue-crack growth thresholds in Ti–6Al–4: role of small cracks. International Journal of Fatigue, vol. 24, pp. 1047-1062, 2002.

[25] A.G. Gavras, D.A. Lados, and J.K. Donald, A unified method of design for fatigue crack growth resistance in structural materials, International Journal of Fatigue, vol. 47, pp. 58-70, 2013.

[26] J.F. McCarver, and R.O. Ritchie, Fatigue crack propagation threlolds for long and short cracks in René 95 nickel-based superalloy, Material Science and Engineering, vol. 55, pp. 63-67, 1982.

[27] D.A. Lados, D. Apelian, and J.K. Donald, Fatigue crack growth mechanisms at the microstructure scale in Al-Si-Mg cast alloys: mechanisms in the near-threshold regime, Acta Materialia, vol. 54, pp. 1475-1486, 2006.

[28] K. Tokaji, and T. Ogawa, The growth behavior of microstructurally-small fatigue cracks in metals, Short Fatigue Cracks, ESIS 13, Edited by K. J. Miller, and E.R. de los Rios, Mechanical Engineering Publications, London, pp. 85-99, 1992.

[29] C.S. Pande, Fatigue of Materials II: Advances and Emergences in Understanding, John Wiley & Sons, Inc., Hoboken, NJ, pp. 3-15, 2012.

[30] M.J. Caton, R. John, W.J. Porter, and M.E. Burba, Stress ratio effects on small fatigue crack growth in Ti-6Al-4V, International Journal of Fatigue, vol. 38, pp. 36-45, 2012.

[31] J.K. Donald, G.H. Bray, and R.W. Bush, An evaluation of the adjusted compliance ratio technique for determining the effective stress intensity factor, Fatigue and fracture mechanics 29, ASTM STP 1332. Philadelphia (PA): American Society for Testing and Materials, pp. 674–695, 1999.

[32] Y. Zhai and D.A. Lados, Microstructure and tensile properties of Ti-6Al-4V and Inconel 718 fabricated by Laser Engineered Net Shaping, Internal report, Integrative Materials Design Center (iMdc), 2015.

[33] G. Lutjering, J.C. Williams, Titanium, Springer, pp 179-181, 2007.